MEDICAL PHYSICS

Experimental helium-beam radiography with a high-energy beam: Water-equivalent thickness calibration and first image-quality results

C. Knobloch[1,2,3] | M. Metzner[1,2,3] | F. Kehrein[1,2,3] | C. Schömers[4] | S. Scheloske[4] | S. Brons[4] | R. Hermann[5,4,6] | A. Peters[4] | O. Jäkel[1,2,4] | M. Martišíková[1,2] | T. Gehrke[5,1,2]

[1]Department of Medical Physics in Radiation Oncology, German Cancer Research Center (DKFZ), Heidelberg, Germany

[2]National Center for Radiation Research in Oncology (NCRO), Heidelberg Institute for Radiation Oncology (HIRO), Heidelberg, Germany

[3]Department of Physics and Astronomy, Heidelberg University, Heidelberg, Germany

[4]Department of Radiation Oncology, Heidelberg Ion-Beam Therapy Centre (HIT), Heidelberg University Hospital, Heidelberg, Germany

[5]Department of Radiation Oncology, Heidelberg University Hospital, Heidelberg, Germany

[6]Goethe University Frankfurt, Institute of Applied Physics, Frankfurt, Germany

Correspondence
T. Gehrke, Department of Medical Physics in Radiation Oncology, German Cancer Research Center (DKFZ), Heidelberg, Germany.
Email: t.gehrke@dkfz.de

M. Martišíková and T. Gehrke share last authorship.

Abstract

Purpose: A clinical implementation of ion-beam radiography (iRAD) is envisaged to provide a method for on-couch verification of ion-beam treatment plans. The aim of this work is to introduce and evaluate a method for quantitative water-equivalent thickness (WET) measurements for a specific helium-ion imaging system for WETs that are relevant for imaging thicker body parts in the future.

Methods: Helium-beam radiographs (αRads) are measured at the Heidelberg Ion-beam Therapy Center with an initial beam energy of 239.5 MeV/u. An imaging system based on three pairs of thin silicon pixel detectors is used for ion path reconstruction and measuring the energy deposition (dE) of each particle behind the object to be imaged. The dE behind homogeneous plastic blocks is related to their well-known WETs between 280.6 and 312.6 mm with a calibration curve that is created by a fit to measured data points. The quality of the quantitative WET measurements is determined by the uncertainty of the measured WET of a single ion (single-ion WET precision) and the deviation of a measured WET value to the well-known WET (WET accuracy). Subsequently, the fitted calibration curve is applied to an energy deposition radiograph of a phantom with a complex geometry. The spatial resolution (modulation transfer function at 10 % —$MTF_{10\%}$) and WET accuracy (mean absolute percentage difference—MAPD) of the WET map are determined.

Results: In the optimal imaging WET-range from ∼280 to 300 mm, the fitted calibration curve reached a mean single-ion WET precision of $1.55 \pm 0.00\%$. Applying the calibration to an ion radiograph (iRad) of a more complex WET distribution, the spatial resolution was determined to be $MTF_{10\%} = 0.49 \pm 0.03$ lp/mm and the WET accuracy was assessed as MAPD to 0.21 %.

Conclusions: Using a beam energy of 239.5 MeV/u and the proposed calibration procedure, quantitative αRads of WETs between ∼280 and 300 mm can be measured and show high potential for clinical use. The proposed approach with the resulting image qualities encourages further investigation toward the clinical application of helium-beam radiography.

KEYWORDS
helium-beam radiography, ion-beam therapy, ion imaging

1 | INTRODUCTION

Transmission imaging with beams of protons and heavier ions has gained large interest in the field of ion-beam radiotherapy over the last two decades.[1-3] The reason for the rising interest is that it has the potential of improving the accuracy of the ion-beam treatment. In multiple theoretical and simulation studies, it has been shown that ion computed tomography (iCT) can provide relative stopping power (RSP) maps of objects with higher accuracy than conventional single-energy X-ray CTs at equal or even lower imaging doses.[4-6] These three-dimensional (3D) RSP maps are essential during treatment planning and delivery of ion-beam therapy.[7] Besides the idea of deploying iCT as planning CT for improving the accuracy of 3D RSP maps, it is also of great interest to detect and minimize deviations between the actual 3D RSP map at the moment of treatment and the one on which the treatment planning is based on. Such deviations might stem from the conversion of Hounsfield units (HU) to RSP maps that was applied to the planning CT, patient misalignment, or anatomical changes during the course of the therapy. Resulting range uncertainties that are related to the HU-to-RSP conversion and to patient misalignment are currently expected to be between $\pm 2.3\%$ and $\pm 2.6\%$ as relative component and additionally ± 1.1 mm as absolute component, considering a confidence interval of about 90% or 1.5σ.[1][8,10,11] With respect to the detection and minimization of such deviations, ion-beam radiography (iRAD) right before treatment fraction application could become a very useful quantitative imaging modality.

First and foremost, it has the potential of verifying the agreement of the integrated RSPs that are directly measured by iRAD in the actual treatment situation (i.e., the patient is already in treatment position on couch right before the treatment fraction) and those from the 3D RSP map of the planning X-ray CT.[12-14] A comparison of a measured 2D water-equivalent thickness (WET) map—that is, the integrated RSP along beam direction with spatial resolution in the plane perpendicular to the beam axis—with the 2D WET map based on the planning CT enables the detection of deviations in WET in the treatment-relevant region above clinical limits. Second, iRAD could simultaneously be used for the alignment during patient setup. This application was suggested for proton radiography early on[14] and over the past 10 years, several studies based on irradiations of a few isolated pencil beams called range probes, or on full radiographs using single-proton tracking were published.[15–18]

These applications of iRAD could potentially be performed at an imaging dose to the patient that is about 10 times lower than for X-ray radiography under the condition of same density resolution and pixel size, referring to studies about proton imaging.[6,14,18,19] For example, the application of daily iRAD would not lead to an increase of dose if the daily orthogonal X-rays for patient alignment can be replaced by iRAD.

In previous works of our group in Heidelberg, we built a prototype imaging system for iRAD consisting entirely of thin silicon pixel detectors called Timepix.[20–22] The system design is unique in the sense that the contrast of the image stems from accurate energy deposition (dE) measurements of individual ions in 300 μm silicon. One advantage is that the detection system can be very thin and compact, which might enable an easier implementation in the clinical environment in the future. Moreover, undesired inelastic nuclear interactions within the detection system are often reduced in comparison to residual energy/range detectors with thicknesses of more than 250 mm.[23-25] This applies to situations in which low-WET regions are imaged using a residual range/energy detector and a high initial energy. The deeper an ion travels into a range detector (i.e., the higher the residual energy of the ion downstream of the object to be imaged), the more likely fragmentation and loss of primary ions is to occur in the detection system, which is not the case for a thin dE detector layer.

The main challenge of using dE measurements in thin layers is the limited WET range within which a high WET resolution can be achieved for a monoenergetic primary ion beam.[21,22] To address that, our long-term aim is to use different initial beam energies for different WET ranges in an approach named energy painting.[22] The iRAD imaging system has mainly been used with helium-ion beams, since we could experimentally demonstrate that helium-beam radiography (αRAD) provides an advantage over proton radiography (pRAD) in terms of spatial resolution without a drawback in WET resolution or imaging dose.[21] The potential advantages of helium ions over protons for ion imaging in general were also shown in several other theoretical and simulation-based studies.[4,26–28] However, further experimental works on helium-ion imaging within the last 10 years are scarce.[29–32]

In the context of αRAD with the above-described system, this contribution focuses on two essential steps toward an envisaged clinical maturity of our method for quantitative imaging of cranial and later in particular abdominal and pelvic body regions.

- First, an establishment of a calibration procedure that connects the measured dE to the corresponding WET of the object to be imaged. A well-established calibration method of the measured signal is key to accurate WET maps. As WET accuracies below 1% should be

---

[1] The calculations of Ref. 8 based on a 95% confidence interval (CI) were adapted to ~90% CI under the assumption of a normally distributed uncertainty. Note that anatomical changes as a source of uncertainty are not included here.[9]

aimed at, usually many effects specific to the given detector have to be taken into account[23,24,33].

In this work, the newly established calibration procedure is demonstrated for homogeneous objects and an object with a more complex, but well-known WET map. The final performance in terms of WET accuracy and precision is determined.

- Second, to enable future transmission ion imaging of thicker body parts with WETs up to 300 mm (e.g., abdomen and pelvis) in the long term, beam energies that exceed the highest therapeutic energy are required. Such energies were recently established at the Heidelberg Ion-beam Therapy Center (HIT). The necessary steps toward this new implementation are briefly described. The specific initial beam energy of 239.5 MeV/u (total range of 355 mm in water) is used to establish a calibration and to measure a radiograph of a phantom with well-known geometry. These measurements were evaluated to answer the question whether objects with WETs up to 300 mm can be imaged with sufficient image quality, especially in terms of spatial resolution and WET precision. Since helium beams with the sufficient energies were not available in ion-beam therapy facilities for a long time, the presented helium-beam radiograph of an object with such a high WET is unique.

2 | MATERIALS AND METHODS

In this work, a calibration curve with the purpose of converting an energy deposition image, as measured by the detection system similar to Ref. 22, into a WET image is established for a beam energy of 239.5 MeV/u, which principally enables the imaging of objects with a WET range of ∼280–310 mm. Furthermore, the performance of the method for an object with a more complex geometry (containing WETs of up to ∼290 mm) is evaluated.

2.1 | Experimental setup

The experimental setup for this work is used to image objects with the detection system depicted in Figure 1, which is the same as first used in Ref. 22. The measurements were performed with helium-ion beams at HIT in the designated room for experiments and quality assurance.
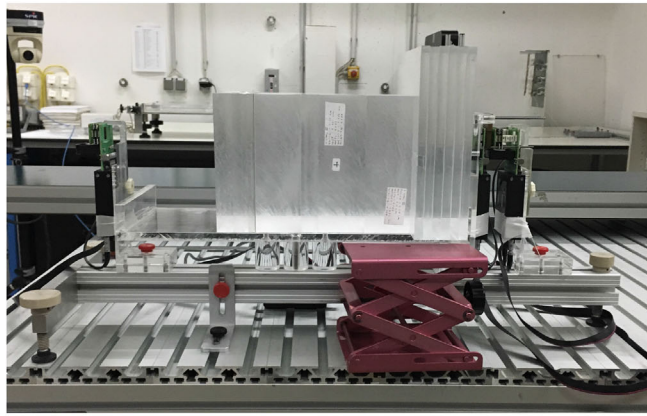
2.1.1 | Detection system

The detection system consists exclusively of thin pixelated TimePix detectors. The TimePix detector was designed by the European Organization for Nuclear Research, and it is a semiconductor hybrid detector with a 256 x 256 pixel matrix (14 mm x 14 mm) and a pixel pitch of 55μm.[34] In this work, the sensitive sensor layer is made from silicon with a thickness of 300μm. Pixel by pixel, the sensor layer is connected via bump bonds to electronic circuits that contain a preamplifier, discriminator, and a digital counter for each pixel. The electronic read-out chip was thinned down from originally 700μm to approximately 100μm in order to minimize multiple Coulomb scattering (MCS) in the detection system.

The Timepix detector is capable of single-particle detection with a detection efficiency close to 100% for ions.[35] In addition to mere detection, further properties of signals caused by incident particles can be measured. While the lateral impact position of the ion on the detector is always measured in the pixelated sensor layer, additionally, either the ion's time of arrival (time), used for data synchronization of the six layers, or dE (energy mode) can be measured. The dE measurement expressed in units of MeV requires a pixel-wise calibration of the measured digital signals. This calibration was performed by ADVACAM (ADVACAM s.r.o., Prague, Czech Republic) based on X-ray radiation.[36] In an earlier work, this per-pixel energy calibration was shown to have an accuracy that is always better than 3% for dE between 4 and 29 MeV/mm, which is the relevant range for αRAD with this system.[37,38] The operation and electronic readout of the Timepix detectors is performed by the read-out interface called FITPIX from ADVACAM.[39] Since measurement and data readout cannot be conducted simultaneously for this Timepix generation, after each active time, which is called a frame (in our case 1 ms) a dead time needed for data readout of the whole pixel matrix follows. For the detection system of this work, where two detectors are connected to one read-out interface, the dead time is approximately 30 ms. During the measurement, the communication with the read-out interface for setting detector parameters, visualizing the raw data online and saving the measured data to a PC, is done by the software Pixet (Version 1.4.7). More details about Timepix detectors and the settings used for this work can be found in Ref. 21.

To determine the entrance/exit positions and directions of single ions at the surface of the imaged object, and to link this track information with the corresponding dE, three pairs of Timepix detectors are required. The first detector pair functions as front-tracking unit, the second one as back-tracking unit, and the third one as energy-deposition unit. All detectors in the front- and back-tracking units as well as the second detector in the energy-deposition unit are operated in time mode. The first detector in the energy-deposition unit is operated in energy mode providing the dE information. The detector pairs are synchronized via trigger signals through a synchronization unit, such that each measurement frame on all six detectors is started synchronously with a maximal time lag of 150 ns. The synchronous measurement of the single ion's time of
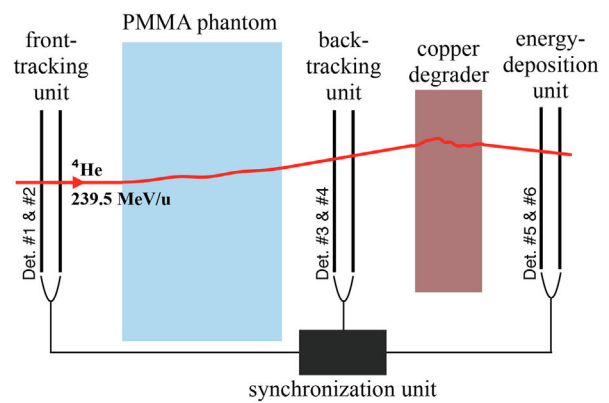
FIGURE 1 (a) Photo and (b) sketch of the experimental setup for the calibration measurements. Plastic blocks with well-known WET can be inserted or removed from the center of the detection system.

arrival in each unit enables the ion tracking based on temporal coincidences with a coincidence window of ± 200ns. Just the matching between signals of the two detectors in the energy-deposition unit relies on spatial proximity with a search radius of 1.1 mm. If two signals are present within this area that is drawn around the impact position at the energy-deposition detector, ion tracking would be ambiguous and the corresponding signals are, therefore, omitted. This happens with a probability of $\sim 6\%$ in the measurements presented in this work.

The detection system also includes a copper energy degrader, as seen in Figure 1b, which is placed between the back-tracking unit and the energy-deposition unit. The function of the energy degrader is to decrease the range of the He-ions behind the back-tracking unit. This enables us to use a higher initial beam energy than the energy corresponding to the imaged WET. The increased helium-ion energy in the object decreases the lateral scattering of the particles, also known as MCS, which allows for a more accurate ion-path reconstruction and consequently, a higher spatial resolution.[22] Copper was found to be a advantageous material to be used as a degrader.[22] However, the WET is dependent on the energy of the particle for low energies[38] and potential consequences on the WET calibration accuracy have to be considered and are investigated specifically for copper.

2.1.2 | Heidelberg Ion-beam Therapy Center

The HIT is the first hospital-based treatment facility for heavy ions in Europe.[40] Since 2009, treatment has been performed with protons and carbon ions. Helium and oxygen ion beams were commissioned in 2013 and 2010, respectively. Therapy at HIT is carried out at three treatment rooms: two of them have a horizontal, fixed beam-line, one is a rotating heavy ion gantry.[41] The experimental room is a fourth beam target which is dedicated to different kinds of research and development. Its equipment is similar to the horizontal treatment rooms, and the same large library of beam parameters is available here. For therapeutic penetration depths between approximately 20 and 300 mm WET, this library contains energy levels in the range of 50.57– 220.51 MeV/u for helium ions. The layout of the HIT-accelerator, however, was planned for carbon ions with an energy of 430.1 MeV/u, which have a penetration depth of ~ 300 mm WET, too.[42] This energy is also the upper energy limit for helium ions, as $^4\text{Helium}^{2+}$ has almost the same charge to mass ratio as the design ion $^{12}\text{Carbon}^{6+}$.

For this experiment, helium beams with an energy higher than the therapeutic ones have been commissioned. This does not require new hardware, higher field strengths, or higher frequencies than used for the therapeutic carbon beams, but it requires an extended data supply. A new set of initial control data for every accelerator device (magnets, RF-devices, beam diagnostics, etc.) has been calculated for a helium beam with 239.5 MeV/u with the existing data supply model. This has been followed by an optimization of the beam parameters, for example, the adjustment of the beam position and width at the beam-target. The accelerator settings for non-therapeutic purposes are stored in the accelerator control system outside the standard library of beam parameters. Thus, they do not affect the latter and are permanently available on demand.

Due to the higher penetration depth than intentionally foreseen when the HIT-facility was built, the existing radiation protection measures had to be reviewed and the permission to produce such beams had to be approved by the authorities.
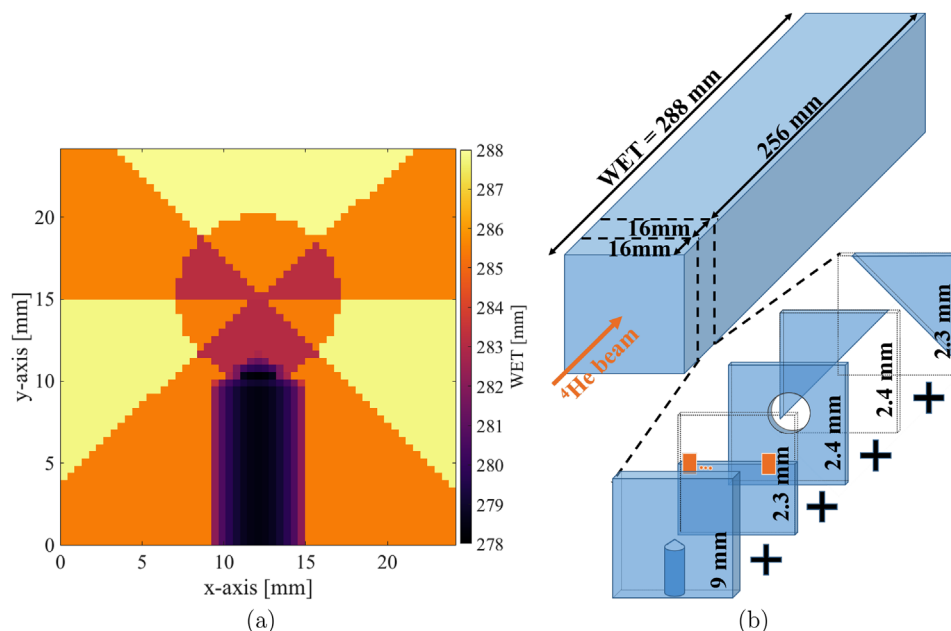
FIGURE 2 Images of the PMMA phantom with complex geometry. Panel (a) shows an exact WET map of the imaging region. The total WET varies between 278.5 and 287.8 mm. Yellow: 287.8 mm, orange: 285.5 mm, red: 283.1 mm, purple: 278.5–282.1 mm. Panel (b) shows a 3D schematic of the phantom (not to scale). Five heterogeneous parts with a maximal WET of 16 mm (part 2 ∩ 4 ∩ 5 = {}) are embedded into two homogeneous blocks of 16.0 and 255.9 mm WET. The diameter of the drilling in the first heterogeneous part is 6mm ≅ maximum reduction of WET by 7 mm. The orange rectangles in part 2 indicate the regions that were used for determining the spatial resolution

2.1.3 | Phantoms

In this work, two different types of phantoms were used:

(i) homogeneous blocks with well-known WET for the calibration measurements and their quality evaluation and

(ii) a phantom with a more complex geometry but still well-known WET for applying the WET-calibrations and evaluating the resulting image quality.

Both were assembled with slabs of varying thicknesses of polymethyl methacrylate (PMMA), also known as acrylic glass. This rigid, transparent plastic offers uniform WET distributions. The WETs of all used PMMA parts were determined by using a variable water column called PEAKFINDER (PTW, Freiburg, Germany).[2] The total phantom WET can be varied by adding or removing PMMA slabs. For the calibration phantoms, homogeneous blocks (i) were used rather than a sloped geometry, as described in Ref. 43. This was done to be able to evaluate the detector homogeneity of the whole sensitive area for each WET studied. The complex geometry (ii), which can be seen in Figure 2b, is constructed with five thin heterogeneous PMMA parts. The WET of this construction

varies between 6.6 and 15.9 mm and is placed at a depth of 16.0 mm WET inside of the phantom, with 255.9 mm WET behind the construction. The phantoms are placed as close as possible to the back-tracking unit, as the ions have a wider angular spread after crossing the phantom than before. This minimizes the number of particles that are lost by not crossing all six detectors.

2.2 | Data postprocessing

The ion path and image reconstruction are both essential for the creation of an iRad with high spatial resolution. Due to the unavoidable MCS of ions, the path of each ion must be known in order to assign the measured dE to the whole path and not only to a single lateral position measured, for example, behind the object.

2.2.1 | Ion path reconstruction

According to the current scientific knowledge, the most-likely path (MLP) reconstruction is the most accurate ion path reconstruction under the condition that the ions' position and direction at the object's front and back surface, and the kinetic energy as a function of depth is given.[44–46] However, the calculations are computationally expensive and, therefore, the cubic spline path (CSP) reconstruction, which is a simpler

---

[2] The PEAKFINDER measurements of the PMMA slabs were partly conducted by Giulia Arico (2016), Lennart Volz (2019), and by the authors (2021).

and faster representation of the MLP, is utilized for this experimental work. The CSP provides an approximation of the position of the particle at any given depth in the object being imaged,[47–49] which is used in the algorithm for image reconstruction. More details about the implementation can be found in Ref. 21.

2.2.2 | Image reconstruction

The image reconstruction is defined here as an algorithm that combines the dE information (or analogously the WET after calibration) measured in the energy-deposition unit with the ion's track information based on the measurements of the tracking units. The reconstruction is performed with an algorithm named Along Path Reconstruction (APR).[21] In short, the object being imaged is divided along the beam axis (z-axis) into 50 intervals of equal thickness. The lateral positions (x-y positions) of each particle at these knots are then determined using the CSP. The WET corresponding to each tracked helium ion is then assigned to the 50 lateral positions at these knots along the particles path, which are in turn projected onto the pixel matrix of the image. Finally, each pixel value of the radiograph corresponds to the mean of the ions' WET values projected onto that pixel. Note that other image reconstruction algorithms for ion radiographs were published before.[50,51] The maximum-likelihood algorithm by Ref. 50 was recently shown to provide better spatial resolution, but on the other hand increased image noise.[52]

2.3 | Establishing a relation between the measured energy loss and the WET of the imaged object

To establish a relation between the measured energy loss and the desired WET of the imaged object, referred to as calibration curve, homogeneous blocks with different WETs were imaged. Each data point used for the calibration curve relates a WET value to the mean of the dE of all reconstructed helium ions, measured in the energy-deposition unit. The maximum WET of a block is defined by the range of the helium-ion beam in water minus the WET of the first five detectors[3] and the copper degrader [4] of the detection system and the elements of the beam nozzle at HIT. Note that this upper limit used for calibration measurements is not necessarily the upper limit of the object's WET for taking a radiograph, since a radiograph should be performed under the condition

---

[3] Ions have to reach and not to cross detector # 6 in order to allow for their track to be reconstructed.

[4] The WET of copper is dependent on the beam energy for very low energies and, therefore, on the object's WET. For this calculation, the lowest possible WET of copper is considered. It corresponds to the lowest possible beam energy at the front surface of the copper degrader, that is, the highest possible WET of the object.

TABLE 1 Helium-beam energy, the corresponding range in water,[53] and the phantom's maximum WET

Energy [MeV/u]	Range in water [mm]	Phantom's maximum WET [mm]
239.5	354.7	316.7

of a high fluence on the last detector # 6 to be dose-efficient. This is described in Section 2.5. The range of such a beam in water and the block's theoretical maximum WET used for the calibration measurements for this beam energy can be found in Table 1. To determine the block's WET at which the fluence of particles on the last detector # 6 is still sufficient (~20% of the fluence on detector # 1) for calibration purposes, measurements starting at the phantom's maximum WET and reducing it in small steps all the while observing the fluence were performed. A WET of 312.6 mm was finally used as a limit for the first calibration measurement.

Following the calibration measurement at the thickest WET, two measurements in small steps of ~3 mm WET were taken to properly sample the steep part of the Bragg peak. Larger steps of 5 and 10 mm WET were used next. The WETs of the homogeneous blocks used for calibration are as follows: 280.58 ± 0.18 mm, 290.70 ± 0.18 mm, 295.51 ± 0.19 mm, 300.86 ± 0.18 mm, 305.68 ± 0.17 mm, 309.26 ± 0.19 mm, and 312.59 ± 0.19 mm. The uncertainty of the WETs stems from the statistical error of the PEAKFINDER measurements and the step accuracy of the PEAKFINDER device.

In theory, the data points should follow the Bethe–Bloch equation. However, this would be a rather complex fit function as there is no closed form of the relation between energy deposition dE and depth z. Instead, a fit function, based on the energy–range relation commonly referred to as Geiger's law and on further calculations by Bortfeld,[54,55] is derived from the measured points to describe the conversion of dE to WET. It yields

$$WET(dE) = R_0 - \left(p \cdot \alpha^{1/p} \cdot dE \right)^{p/(1-p)}, \quad (1)$$

where R_0, p, and α are handled as free fit parameters in a nonlinear least square method called trust-region method. Note that the inverse of that function is commonly used to describe the energy deposition of a single ion over its penetration depth. Furthermore, dE in Equation (1) is the energy deposited in the detection system and defined as a positive number. A plot of $WET(dE)$ is shown in Figure 3. In theory, R_0 would correspond to the WET range R_{exp}, as defined in Section 2.5.1, minus the total WET of the experimental setup. However, since the actual physics of this experiment might be more complex than expressed by the mathematical model, R_0 is left as a free parameter to allow for more flexibility.
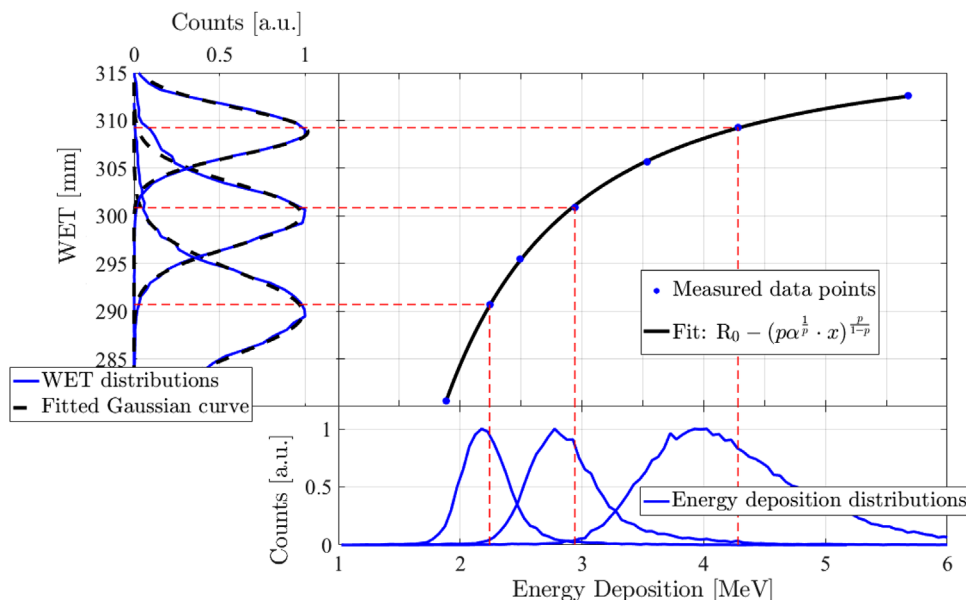
FIGURE 3 Calibration curve created with the fitted function, which can be used to convert dE values measured behind an object into their corresponding WET. For phantom WET values of 290.70, 300.86, and 309.26 mm, the figure additionally shows the normalized single-ion energy deposition distributions (below the calibration curve), and the corresponding single-ion WET distributions, converted with the fitted calibration curve (to the left of the calibration curve). Single-ion WET distributions are fitted with Gaussian curves. Error bars are omitted, as they are smaller than the data points. The WET uncertainties are ~ 0.18 mm (resulting from the uncertainty of the range-pullback measurements) and the dE uncertainties are between $1.1 \cdot 10^{-3}$ and $6.6 \cdot 10^{-3}$ MeV (resulting from the error of the mean of the distribution).

2.4 | Evaluation of the calibration quality

To investigate whether the calibration curve can reliably convert the measured dE of all reconstructed helium ions to a WET image, the single-ion WET precision as well as the WET accuracy are determined. The definitions are as follows:

2.4.1 | Single-ion WET precision

Currently, it is a common practice to use the WET distribution of single ions instead of a WET distribution of pixel values to assess the precision. This is because the single-ion distribution is not dependent on pixel size nor on imaging dose,[23,25,56] which enables an easy and direct comparison of different detection systems or methods. In this work, the energy deposition of each He-ion after having crossed a homogeneous phantom is converted to a WET value using the established calibration curve. All He-ions whose paths are inside a region of 11.5 mm x 11.5 mm on the surface of the detector are then considered for the generation of a WET distribution.[5] A Gaussian curve is fitted to this distribution

in order to determine the standard deviation σ. The relative single-ion WET precision σ_{WET} is then calculated with the following equation:

$$\sigma_{\text{WET}} = \frac{\sigma}{WET_{\text{GT}}}, \qquad (2)$$

where WET_{GT} refers to the ground truth WET determined by range-pullback measurements (cf. Section 2.1.3). The uncertainty of the precision is quantified by the error of the Gaussian fit.

To determine the single-ion WET precision for as many different WETs as possible, the measurements for assessing the accuracy are used as well as the measurements used to establish the calibration curve. Since the precision values are not at regular WET intervals, the trapezoidal rule is applied and then divided by the WET interval to determine the mean of the precision values.

A conversion of the precision value presented in other works is only needed if the WET precision of imaging modalities with different ion types is to be compared, since different ion types have a different extent of range straggling ($\sigma_{\text{RS}} \approx 0.012 R^{0.951} \sqrt{A}^{-1}$, where R is the total range and A is the ion's mass number[57,58]). In this work, helium-ion (α) imaging is compared to proton (p) imaging using the following conversion of single-proton WET precision ($\sigma_{\text{WET,p}}$) based on Ref. 23

$$\sigma_{\text{WET},\alpha} = \sqrt{\left(0.5 \cdot \sigma_{\text{RS,p}}\right)^2 + \left(\sigma_{\text{WET,p}}^2 - \sigma_{\text{RS,p}}^2\right)}, \qquad (3)$$

---

[5] Since the APR image reconstruction is used, each particle contributes 50 dE values that are assigned to 50 lateral positions along the path to an image. When selecting the homogeneous region, the dE values corresponding to a lateral position (x-y-plane) of an ion are only considered if this position is inside the region of interest.

where WET precision and range straggling is defined relative to the object's WET and total range in units of %, respectively. The underlying assumption is that the range straggling of helium ions is reduced by a factor of 2 compared to protons, whereas other contributions related to the detection system (the second term below the square root) are constant, that is, assuming that a detection system for proton imaging works equally well for helium-ion imaging and vice versa.

2.4.2 | WET accuracy

To determine the WET accuracy, it is important to use measurements that are independent of the calibration curve, that is, not used when creating the fit for the calibration curve. Therefore, three additional measurements of homogeneous blocks were performed independently of the calibration procedure. After determining the WET distribution and the corresponding Gaussian fit for these measurements as described above, the WET accuracy is calculated based on the expected value of the Gaussian distribution μ. The deviation of μ to the ground truth WET, WET_{GT}, of the phantom gives the absolute WET accuracy, while the relative accuracy ΔWET_{rel}, determined by dividing this value by WET_{GT}, gives the deviation in percent:

$$\Delta WET_{rel} = \frac{\mu - WET_{GT}}{WET_{GT}}. \qquad (4)$$

The phantom WET values used to determine the accuracy are: 287.39 ± 0.18 mm, 303.18 ± 0.17 mm, and 311.47 ± 0.17 mm. They are evenly distributed along the WET range of the calibration curves.

2.5 | WET map measurement of a phantom with a complex geometry

To evaluate the performance of the calibration curve for measuring a quantitative WET map, a phantom with a more complex geometry, of which all components have a well-known WET, is imaged with the same detection system. Using the fitted calibration curve, the measured energy deposition of tracked helium ions is converted to a WET map. The ground-truth map of the used phantom can be seen in Figure 2 with a pixel size of $440\mu m$ x $440\mu m$. The total WET of the phantom varies between 278.5 and 287.8 mm. This WET range is situated at the lower WET range of the calibration curve. The reason for this is explained below.

2.5.1 | Object's maximum WET of the calibration curve for the purpose of radiography

For a successful application of a WET calibration, not only the calibration function is important but also a definition of a WET range within which the calibration function of a certain initial energy should be used. An upper limit WET_{max} is given by the fact that for total WETs (i.e., the sum of all WETs within the beam path up to detector # 6 of the detection system) close to the beam's range, the ion fluence at detector # 6 drops drastically. Under such conditions, the majority of the ions cannot be tracked on all six detectors and do not contribute to the radiograph. In a clinical application, this would lead to unnecessarily high imaging doses for a desired quality of the WET-map. Therefore, the helium-ion fluence Φ of the six detectors was evaluated for all 10 calibration measurements and each data point was plotted as a function of WET, and the following function was fitted for the data points

$$\Phi(WET) = [1 - a \cdot WET][0.5(\mathrm{erf}\,(b(c - WET)) + 1)], \qquad (5)$$

where a, b, c are free fit parameters and erf is the error function. The linear function in the first square bracket reflects the attenuation due to inelastic nuclear interactions and scattering, and the second bracket models the range straggling at the end of the ions' range. Like this, the R_{exp} (defined as inflection point of $\Phi(WET)$) was determined experimentally. Based on that, WET_{max} was calculated as follows:

$$WET_{max} = [0.97 \cdot R_{exp} - (5 \cdot WET_{detector} + WET_{beam\ line}$$
$$+ WET_{copper})] \cdot (1 - 2 \cdot \sigma_{WET,max}), \qquad (6)$$

where $WET_{detector}$, $WET_{beam\ line}$, and WET_{copper} are the WETs of the corresponding components and $\sigma_{WET,max}$ is the single-ion WET precision at WET_{max} determined during the evaluation of the quality of the calibration curves.

Three percent of the range was subtracted to assure that the fluence has not considerably dropped. Figure 5 shows that at 97% of R_{exp}, the fluence of the particles is at 80%, which ensures that the 80% fall-off is certainly downstream of detector # 6. Afterward, the WET of all elements besides the object to be imaged is subtracted. Last, another $2 \cdot \sigma_{WET,\ max}$ is subtracted to assure that at least 2σ of the WET distribution corresponding to WET_{max} can be measured without suppressing high-WET contributions by incipient stopping of ions upstream of detector # 6.

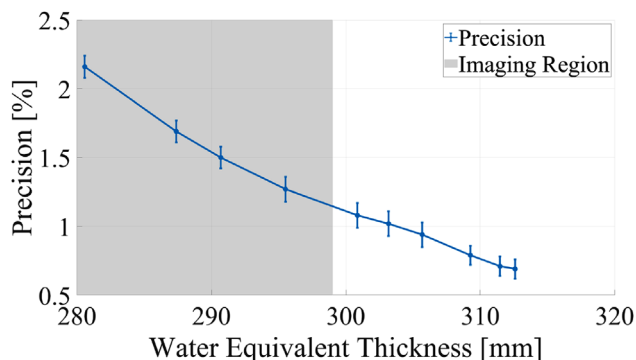For assessing the final quality of the radiograph, we examine both the spatial resolution and the WET accuracy.

FIGURE 4 Single-ion WET precision in %. The precision improves (i.e., decreases) for higher WET of the homogeneous block. The precision values for data converted with the fitted calibration curve are shown.

2.5.2 | Spatial resolution

The spatial resolution is evaluated using the same method as in Ref. 21 based on a slanted edge,[59,60] which enables the determination of the spatial resolution without limitations by pixel sizes. After oversampling, an error function is fitted to the resulting edge spread function. It is then numerically differentiated, which gives the line spread function (LSF). A Fourier transform finally yields the MTF. The MTF $_{10\%}$ gives the spatial frequency at 10 % of the maximum MTF and is a common measure for spatial resolution.[61,62] Ten line sections crossing the horizontal edge (Figure 2b) within the radiograph were assessed and the mean and standard uncertainty of the MTF $_{10\%}$ values is reported.

2.5.3 | WET accuracy of the measured radiograph

The WET accuracy is determined by calculating the difference of the measured WET-map to a blurred ground-truth image. To minimize the influence of the spatial resolution on the reference WET-distribution as much as possible during the assessment of the WET accuracy, the ground-truth image GT was first convolved with a Gaussian blur filter to produce the blurred ground-truth image GT_{blur}. The standard deviation of the Gaussian blur filter was determined as the standard deviation of the LSF of the measured radiograph. A relative difference map $I_{\Delta,rel}$ is calculated pixel-wise with the following equation:

$$I_{\Delta,rel} = \frac{\alpha Rad - GT_{blur}}{GT_{blur}} \cdot 100\%. \quad (7)$$

The result is used to determine a pixel WET distribution to calculate the mean, MAPD, and root-mean-square deviation (RMSD). MAPD is the mean of the

absolute values of the difference distribution, and RMSD is defined as the square root of the average of squared differences. Both are defined by the relative differences, that is, in units of %.

3 | RESULTS

The results concerning the quality of the calibration curve (dE-to-WET) in terms of WET precision and accuracy are described. In the last part, the measured WET map of a more complex object with WETs of up to $\sim$ 290 mm obtained by applying the calibration curve is evaluated.

3.1 | WET calibration curve

Equation (1) is fitted to the measured data points to determine a calibration curve, as described in Section 2.3. Table 2 shows the calculated fit parameters, which were handled as free parameters. $R_0 = 317.5$ mm is approximately equal to the range of the helium ions minus the WET of the detection system and beam line ($353.9 - 38.0 = 315.9$ mm). The corresponding function is depicted in Figure 3. The figure shows both the calibration curve, fitted to the measured data, as well as the normalized single-ion energy deposition distributions (shown in the panel below the curve), the single-ion WET distributions, and their corresponding Gaussian fits (shown in the panel to the left of the calibration curve) for three blocks with a homogeneous WET (290.7, 300.86, and 309.26 mm). For increasing WET, the energy deposition distributions become wider, while the WET distributions become narrower.

To determine how well the fit describes the data, the root mean square error (RMSE) is calculated to be as low as 0.18 mm and the adjusted R^2, $R^2_{adj} = 0.9997$,[6] is very close to unity (Table 2). They indicate that the fit is in very good agreement with the measured data and, therefore, this fit can be considered as one valid option for establishing the WET calibration.

3.1.1 | Single-ion WET precision

The single-ion WET precision is calculated for all 10 measurements of the homogeneous WET blocks. In Figure 4, the precision for each energy can be seen as a function of the WET. The precision improves with increasing WET of the block. This characteristic can also

---

[6] The adjusted R^2 or adjusted coefficient of determination is defined as $R^2_{adj} = 1 - \frac{SSE}{SST}(\frac{n-1}{n-p})$, where SSE and SST are the residual sum of squares and the total sum of squares. In contrast to R-squared, the ratio of SSE and SST is weighted by the factor $(n-1)/(n-p)$, with n as the number of observations and p as the number of fit parameters.

TABLE 2   Fit parameters with their uncertainties (1σ) and quality measures of the fit

R_0 [mm]	α	p	adj. R^2	RMSE [mm]
(317.5 ± 0.5)	$(5.3 \pm 2.5)\ 10^{-4}$	(2.21 ± 0.08)	0.9997	0.18

TABLE 3   Absolute and relative accuracy for three WET thicknesses using the fitted calibration curve to convert the single-ion energy deposition values into the WET distribution

WET [mm]	287.39	303.18	311.47
Absolute accuracy [mm]	(-0.91 ± 0.03)	(-0.76 ± 0.02)	(-0.36 ± 0.02)
Relative accuracy [%]	(-0.32 ± 0.01)	(-0.25 ± 0.01)	(-0.12 ± 0.01)

be recognized in Figure 3, where the width of single-ion WET distributions decreases for higher WETs of the calibration phantom. The measured precision values vary between $0.69 \pm 0.01\%$ (highest WET) and $2.16 \pm 0.01\%$ (lowest WET). The precision mean for the fitted calibration curve, considering WET values up to 300.86 mm, slightly above the maximum WET calculated by Equation (6), is $\bar{\sigma}_{WET} = 1.55 \pm 0.00\%$.

3.1.2 | WET accuracy

Three independent measurements of homogeneous blocks with WET values between the data points used for establishing the calibration curve were performed to calculate the WET accuracy. The dE values of the single ions were converted to WET distributions with the calibration curves, and then Equation (4) was applied to calculate the WET accuracy. The results can be found in Table 3. The absolute/relative accuracy does not exceed -0.91 ± 0.03 mm/$-0.32 \pm 0.01\%$. The best (smallest) accuracies are found for the largest WET. All three measurements show a slight underestimation of WET after the application of the calibration. This is discussed in Section 4.2.

3.2 | A WET map measurement of a complex object

A helium-beam radiograph of a phantom with a more complex—but well-known—WET composition between 278.5 and 287.9 mm was performed and evaluated. The WETs were chosen to be below the upper limit, WET_{max}, of the WET range within which the calibration function can be used for dose-efficient imaging (cf. Section 2.5.1). The underlying measured fluence and the fit model for the experimental determination of the range R_{exp} are shown in Figure 5. R_{exp}, defined as inflection point in the fall-off, was determined to be 353.9 mm and the calculation according to Equation (6) yields $WET_{max} \approx 299$ mm for the established calibration curve corresponding to the initial beam energy of 239.5 MeV/u.
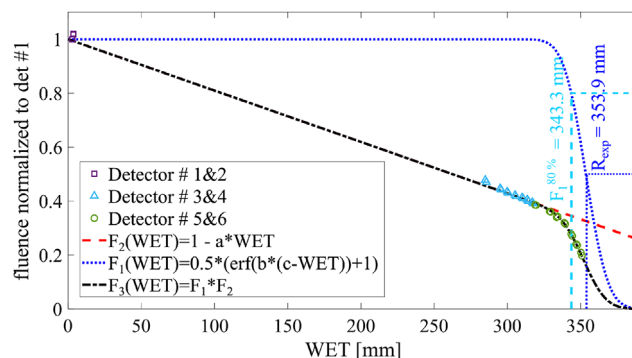

FIGURE 5   Helium-ion fluences measured at the detectors # 1 to #6 that are normalized to the fluence at detector # 1. Measurements of 10 different WETs of the homogeneous calibration blocks (data points) and the chosen fit model (black, dashed-dotted) are shown. The blue dotted vertical line indicates the experimentally determined range R_{exp} and the light blue dashed vertical line marks the 80% fall-off of F_1.

The measured energy deposition image is calibrated to a WET image using the fit function. The resulting WET map of the phantom after having conducted the whole data processing chain (cf. Section 2.2.1) can be seen in Figure 7b. The ground-truth image can be seen in Figure 2.

3.2.1 | Spatial resolution

The spatial resolution is evaluated using the horizontal slanted edge within the measured radiograph, as described in Section 2.4 and detailed in Ref. 21. The mean and the standard uncertainty of the modulation transfer function at 10% of the maximum ($MTF_{10\%}$) for the evaluation of 10 line sections was 0.49 ± 0.03 lp/mm. As intermediate steps to this result, one exemplary oversampled edge spread function (oESF), the corresponding fit with the error function and the resulting MTF, is shown in Figure 6. Although the oversampling did not work perfectly due to a too small angle between pixel matrix and edge orientation, approximately 60% of the original pixels with an already small pixel pitch of 0.44
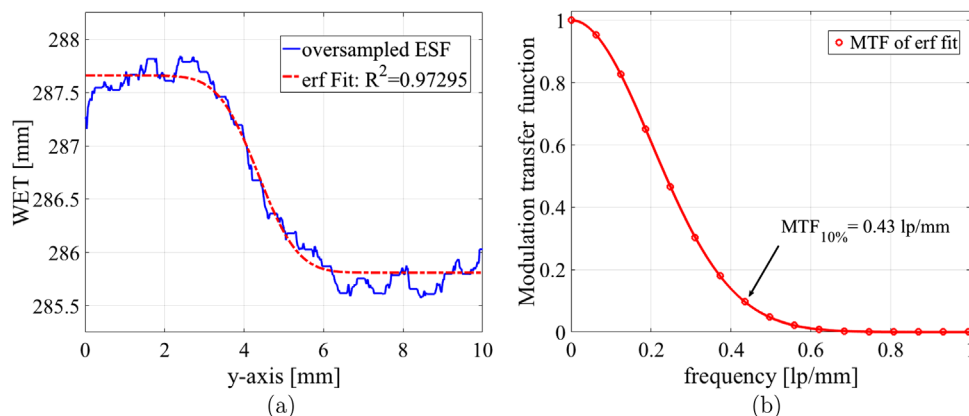
FIGURE 6   Panel (a) shows one of the 10 oversampled edge spread functions (oESF) and (b) the corresponding modulation transfer function (MTF) used to determine the spatial resolution as MTF $_{10\%}$.

mm were oversampled and provided a sufficient number of sampling points along the edge spread. Additionally, for further evaluation of the accuracy of the radiograph, the standard deviation of the LSF is determined to be $\sigma_{LSF} = 0.73 \pm 0.04$ mm. This value is used for a Gaussian blur filter to be applied to the ground-truth image. In good approximation, it creates a ground-truth image with the same spatial resolution as measured in the WET map. This allows for an accuracy assessment that is independent of spatial resolution.

3.2.2 | WET accuracy of measured WET map

The relative difference image $I_{\Delta,rel}$ between the blurred ground truth and the measured WET map is calculated with Equation (7) and can be seen in Figure 7c. The white pixels that are predominant indicate relative differences below $\pm 0.5\%$. For the low-WET regions of the image (WETs below ~ 280 mm), a slight systematic overestimation, indicated as red pixels, is observed. However, the light red pixels that are the great majority of all red pixels still have relative differences below 1%.

A histogram of the relative pixel differences between the two images is finally shown in Figure 7d. The mean of the distribution is 0.1% and more importantly, the mean absolute percentage difference (MAPD) is only 0.21%. For completeness, the root-mean-square difference (RMSD) was calculated to be 0.29%.

4 | DISCUSSION

In this work, a dE-to-WET calibration was established for a helium-ion imaging system exclusively built from thin silicon pixel detectors using newly implemented helium beams at the HIT, which exceed the therapeutic energies. In Sections 4.1 and 4.2, the calibration method

and its quality are discussed to address the question whether the unique way of image formation based on dE measurements in 300μm silicon can produce image qualities that are similar to the ones of state-of-the-art ion imaging systems using residual energy and/or range detectors. An outlook regarding solutions of technical challenges is given in Section 4.3. Section 4.4 discusses whether αRAD of objects with WETs close to 300 mm still yields sufficient spatial resolution, which is of interest for an envisaged iRAD of abdominal and pelvic regions.

4.1 | Choice of the calibration method

The fit with only three parameters (cf. Section 1) based on Ref. 54 was chosen due to its practicability and the fact that it describes the mean dE as a function of WET for perfect detectors. The main concern with the fit is that the experimental setup introduces unknown effects on the underlying physics (e.g., signal saturation of dE measurements or perturbations due to the energy-dependent WET of copper) that could cause the fit function to no longer describe the measurements adequately. However, the adjusted R^2 value of the performed fit was found to be 0.9997 (Table 2). This value is very close to 1 and proves the fit to be a viable option for the WET calibration. The potential disadvantage that the fitted curve does not perfectly cross all measured data points turns out to be negligible, since the RMSE of the fit, which is only 0.18 mm, indicates that the calibration function is very close to the measurements. Alternatively, an interpolation to define the calibration function was considered as it fully respects the data points as measured ground truth and does not rely on a model that might provide an oversimplified calibration function. However, slight inaccuracies during the calibration process even for one single data point can have a much larger impact on the surrounding section of the curve and dE values outside of the range of measured data
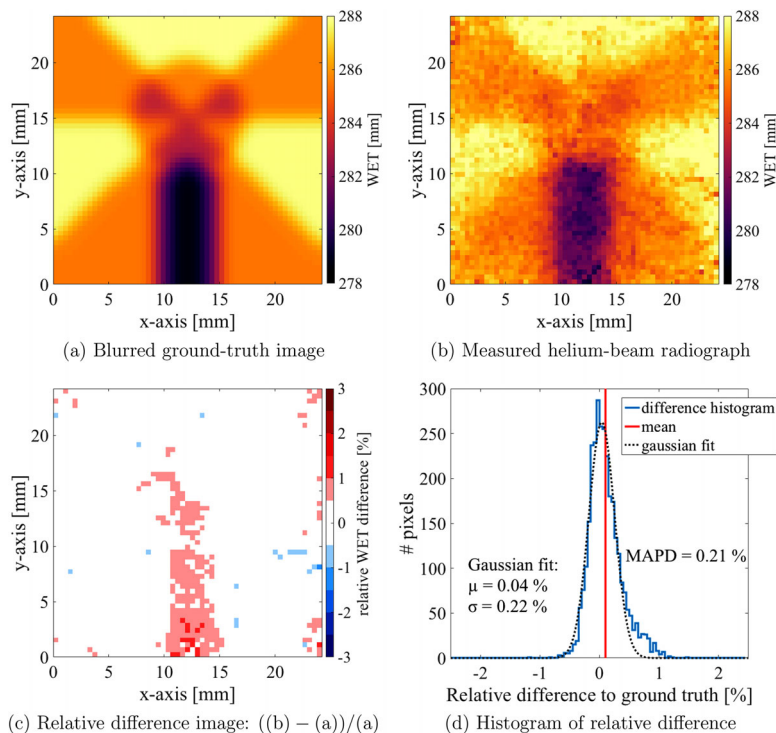
(a) Blurred ground-truth image

(b) Measured helium-beam radiograph

(c) Relative difference image: $((b) - (a))/(a)$

(d) Histogram of relative difference

FIGURE 7 (a) The ground-truth image after application of a Gaussian blur filter with $\sigma = 0.73$ mm that corresponds to σ_{LSF} of the measured radiograph, (b) the measured radiograph of the phantom using the fitted calibration curve to convert the dE image to a WET image, (c) the relative difference image of the measured radiograph to the blurred ground-truth image, and (d) the histogram of the relative differences between the blurred ground-truth image and the measured radiograph with an MAPD of 0.21%.

points cannot be converted to WET. This results in a reduction of the WET range that can be imaged. At this point, it is important to mention that a calibration curve using the Piecewise Cubic Hermite Interpolation Polynomial, as a built-in MATLAB (Version 9.6.0 [R2019a]) function, was also established; however, the quality of said calibration curve was not deemed advantageous compared to that of the fitted curve. Therefore, it is not presented in this work, as the characteristic limitations of the interpolated curve conclude that using the fitted curve for the image calibration is favorable.

4.2 | Quality of the calibration curves

4.2.1 | Single-ion WET precision

The single-ion WET precision (σ_{WET}) decreases (meaning it improves) with increasing WET of the homogeneous blocks. This is a result of the shape of the calibration curve, which in turn is caused by the typical behavior of dE in dependence of the crossed material depth (the higher the WET, the larger the measured dE differences for small WET changes). The flatter the calibration curve, the narrower the single-ion WET distribution becomes. For our measurements, σ_{WET} varies from 2.16% to 0.69%. Note that the best (lowest) precision value at WET ≈ 313 mm is close to the best possible precision for ^{4}He ions, which is given by the intrinsic range straggling of 0.55%. The worst precision value of 2.16% was measured at an approximately 30 mm smaller WET, which has implications on the

envisaged concept of energy painting, as discussed in Section 4.2.3.

The mean of the precision values is $1.55 \pm 0.00\%$, when calculated for the WET range between 280.58 and 300.86 mm that is relevant for measuring WET maps as determined using Formula (6).

4.2.2 | WET accuracy

For three additional measurements (not used for establishing the calibration curve, i.e., independent), the worst (largest) accuracy value was -0.91 ± 0.03 mm ($-0.32 \pm 0.01\%$ relative to block's ground-truth WET value). The deviation from the ground truth is so small that it will hardly matter for the overall WET uncertainty, as the mean WET precision of 1.55% dominates by far.

On closer inspection, it is apparent that there is a small systematic uncertainty, as all accuracy values are negative. This means that the expected value of the Gaussian WET distribution μ is systematically smaller than the ground truth and the WET is slightly underestimated. It is due to the fact that for establishing the calibration curve, the mean of dE measurements is taken, whereas when using the calibration curve, single-ion dE values are first converted to WET, after which the expected value μ is determined. The combination of nonlinear calibration functions and the rather broad energy deposition distributions causes this systematic uncertainty. The magnitude of this uncertainty can easily be determined with the measurements used for the calibration curve. For the three WET distributions (cf. Section 3), the

relative difference between μ and the ground-truth WET value is 0.31% (290.70 mm), 0.25% (300.86 mm), and 0.15% (309.26 mm). Since this uncertainty is small, it is tolerated in the scope of this work. However, it should be noted that an implementation of a correction would presumably further improve the WET accuracy.

4.2.3 | Comparison of the WET precision with other studies

A plausibility check of the found single-ion WET precision values is possible by comparing them to the WET precision values previously measured in our work.[22] The same experimental setup (including a ~6 mm-thick energy degrader out of copper), but a helium-ion beam with a significantly lower beam energy of 185.3 MeV/u, was used. For a WET range from 158 to 160 mm, a mean precision of 1.26% was previously achieved. The precision of this work within the WET region (280.58 and 300.86 mm) that can be used for imaging varies between 1.08% and 2.16%. Since the best found precision values of the WET range are close to each other (15% difference) and the determination of the "sweet spot" (highest WET precision without measuring at detector #6 in the steep fluence drop) was less accurate for the previous work, the observations are in good agreement.

Further studies using different detection setups have determined precision values for proton beams[23] experimentally and for helium ions in Monte Carlo simulations.[25] After converting the precision using Equation (3) if needed (protons) and calculating the average of a 20 mm WET range that is as close as possible to the investigated WET range of this study, the mean WET precision values can be compared.

To our knowledge, the best reported measured single-ion WET precision that has been achieved is 1.35% for a WET range of (219.7 and 239.9 mm).[23] This corresponds to a helium-ion precision of 0.95% after conversion and under the assumption that the detection system would provide the same performance (e.g., in terms of quenching or suppression of fragmentation background) for helium ions as for protons.

For a simulation study about helium-ion imaging with a tracking calorimeter, which also includes higher WET ranges up to ~310 mm, a simulated helium-ion precision as low as 0.9% for the same WET range of (280.86 and 299.8 mm) can be extracted.[25]

For a completely fair comparison, the simulations and assumptions have to be experimentally verified. However, it can give a first indication on how the measured WET precision values compare to a state-of-the-art and a future imaging system.

The precision values from other studies are at maximum 40% better than the measured mean WET precision of 1.55% of this work. Considering the dE

measurement of this work is performed within $300\mu m$ silicon, while the residual energy and/or range is measured in detection systems with thicknesses above 250 mm,[23,25] the observed WET precision is surprisingly close to the best precision achieved until now. Furthermore, the comparison shows that an extension of the WET range toward WETs below 280.58 mm should not be performed using the same initial energy, since the WET precision deteriorates quickly. As a consequence, a WET range between 0 and 300 mm would require approximately 15 different initial energies (each one covering a WET range of approximately 20 mm) for the concept of energy painting. This amount of WET calibrations for the different initial energies seems feasible.

Finally, a pixel WET precision under the assumption of a moderate fluence of 10 helium ions per pixel computes to $1.5 \cdot \frac{1.55\%}{\sqrt{10}} = 0.74\%$ (1.5σ), which compares well to the expected range uncertainties of ~2.45% (1.5σ) in ion-beam therapy.[8,10]

4.3 | Outlook: solutions of technical challenges toward an envisaged clinical application

The suggested concept of energy painting could time-efficiently be implemented at HIT, if a multi-energy operation mode is established.[63] However, there are additional technical challenges associated with the detection system that must be resolved prior to an envisaged clinical implementation:

(i) The active areas of the six detectors currently limit the field of view to ~2 cm^2, if the object to be imaged cannot be moved in the plane perpendicular to the beam axis. To overcome this limitation, the detection system could be mounted on a 2D moving stage. The pencil-beam scanning at HIT could then be synchronized with the stage movement to measure large field-of-view radiographs.

(ii) The Timepix technology in combination with the used read-out interface FITPIX provided a high rate of dead-time of 97%. Such dead-time rates are not suitable for a time-efficient implementation of iRAD. Next-generation Timepix technologies, named Timepix3 and 4[64,65] with practically dead-time free acquisition due to data-driven, sparse readout of the pixel matrix, could be used to address this challenge. Timepix3 and 4 enable hit rates of ~40Mhits/s/cm^2 350Mhits/s/cm^2. With these rates, helium-ion detection rates higher than 1 MHz and image acquisition times on the order of seconds are conceivable.

(iii) In this work, the matching between signals of detector #5 and #6 in the energy-deposition unit relies on spatial matching with a search radius of 1.1 mm, since detector #5, operated in energy mode, cannot

measure the ions' time of arrival. To avoid ambiguities for ion tracking, an upper limit of the fluence rate of $\sim 25 \cdot 10^3$ ions/s/cm^2 should not be exceeded. This limitation will be resolved by using Timepix3&4 technology that can enable energy-deposition and time-of-arrival measurements simultaneously. The new limits will be solely determined by the time resolutions and will be above the fluence rate limits mentioned in (i).

4.4 | A WET map measurement of a complex object

After application of the fitted calibration curves, the image quality of a WET map of a more complex phantom was evaluated. Although the oversampling with a slanted edge did not work perfectly, due to a too small angle of 1 ° between the principle axes of the pixel matrix and edge orientation, approximately 60% of the original pixels with an already small pixel pitch of 0.44 mm were oversampled and provided a sufficient number of sampling points along the edge spread. The MTF $_{10\%}$ was found to be 0.49 $\pm$ 0.03 lp/mm at a WET of 285.5 mm/287.8 mm. A comparison to other studies is not readily possible, since—to our knowledge—ion radiographs of such high WETs were not yet measured. The spatial resolution for head sized objects of our previous work ranged from MTF $_{10\%}$ = 0.54 to 0.69 lp/mm depending on the thickness of the energy degrader. A recent study on helium-beam imaging with the phase II detection system of the U.S. pCT collaboration reported a spatial resolution of MTF$_{10\%}$ = 0.61 lp/mm for helium-beam radiography (α RAD), however, at an approximately three times lower phantom's WET of $\sim$100 mm, where the ions have undergone less scattering events.[29]

Using the Nyquist theorem, the spatial resolution governed by the pixel size of an X-ray CT scanner can be calculated to assess whether the achieved spatial resolution is sufficient for an envisaged clinical application. Assuming a voxel length of $D = 1.5$ mm, which is already small for X-ray CT imaging of pelvic or abdominal sites,[66,67] the spatial resolution is MTF $_{10\%}^{CT,1.5 \ mm} = \frac{1}{2 \cdot D} = 0.33$ lp/mm. Hence, the spatial resolution measured in this work (determined independently of pixel size) is better than that of X-ray CT imaging (limited by slice thickness) currently used for treatment planning in the pelvic/abdominal region.

The MAPD of 0.21% and RMSD of 0.29%, which are a measure of WET accuracy of the WET map based on αRAD, compare well to other studies. Both Refs. 32 and 68 imaged cylindrical phantoms with different inserts using helium-ion CT. Reference 68 used a phantom with a diameter of 100 mm and achieved an MAPD of 0.68% and an RMSD of 0.78% by comparing measured RSPs

to ground-truth RSPs in homogeneous regions voxel-by-voxel, while Ref. 32 used a phantom with a diameter of 150 mm and achieved an MAPD of 0.3%. Another recent study on proton radiography with a prototype clinical system reported WET accuracies below 0.33% for various inserts inside a head phantom, which is again very much in line with our findings.

5 | CONCLUSIONS

This work focuses on the establishment of a procedure to convert measured energy deposition (dE) of single helium ions to quantitative WET maps of objects to be imaged, using a unique ion-imaging system and a helium beam with an energy of 239.5 MeV/ u. This exceeds therapeutic energies and is suitable for imaging of thicker body parts with WETs of up to 300 mm (such as abdomen and pelvis) in the future if the image quality is sufficient for an envisaged clinical application at such large WETs.

The mean single-ion WET precision of 1.55% corresponds to a pixel's WET precision of $1.5 \cdot \frac{1.55\%}{\sqrt{10}} = 0.74\%$ (1.5σ, assuming 10 He-ions per pixel). Comparing this to currently expected range uncertainties of $\sim$2.45% in ion-beam therapy shows that an envisaged treatment verification based on this imaging system has high potential. Of course, this requires an extension of the WET range that can be imaged with high precision. We plan to overcome this current limitation by means of energy painting, that is, using different initial energies for different subregions of a larger image.

For the measured WET map, the mean absolute percentage deviation (MAPD) of 0.21% compares well with other recent studies on helium-ion CT and proton radiography. The spatial resolution of MTF$_{10\%}$ = 0.49 $\pm$ 0.03lp/mm for object with WETs of $\sim$290 mm is superior to that of an imaging modality with a voxel length of 1.5 mm, which is already considered small for X-ray CT imaging of the abdominal and pelvic region. This supports the assessment that ion imaging could be of great use in ion-beam therapy.

Overall, these findings show that helium-beam radiography with the presented detection system has potential for a clinical application, even for projections/WET maps of thicker body parts.

CONFLICT OF INTEREST

The authors have no conflicts to disclose.

DATA AVAILABILITY STATEMENT

The data supporting the results of this study are available upon reasonable request to the corresponding author.

REFERENCES

1. Johnson RP. Review of medical radiography and tomography with proton beams. *Rep Prog Phys*. 2017;81:016701.
2. Poludniowski G, Allinson NM, Evans PM. Proton radiography and tomography with application to proton therapy. *Br J Radiol*. 2015;88:20150134.
3. Parodi K. Heavy ion radiography and tomography. *Phys Med*. 2014;30:539-543.
4. Meyer S, Kamp F, Tessonnier T, et al. Dosimetric accuracy and radiobiological implications of ion computed tomography for proton therapy treatment planning. *Phys Med Biol*. 2019;64.
5. Arbor N, Dauvergne D, Dedes G, et al. Monte Carlo comparison of X-ray and proton CT for range calculations of proton therapy beams. *Phys Med Biol*. 2015;60:7585-7599.
6. Schulte RW, Bashkirov V, Loss K MC, et al. Density resolution of proton computed tomography. *Med Phys*. 2005;32:1035-1046.
7. ICRU. 6. Treatment Planning. *Report*. 2016:1473-6691.
8. Yang M, Zhu XR, Park PC, et al. Comprehensive analysis of proton range uncertainties related to patient stopping-power-ratio estimation using the stoichiometric calibration. *Phys Med Biol*. 2012;57:4095-4115.
9. Lomax AJ. Myths and realities of range uncertainty. *Br J Radiol*. 2020;93:20190582.
10. Paganetti H. Range uncertainties in proton therapy and the role of Monte Carlo simulations. *Phys Med Biol*. 2012;57:R99-R117.
11. Taasti VT, Baumer C, Dahlgren CV, et al. Inter-center variability of CT-to-SPR conversion in particle therapy: survey-based evaluation. *Radiother Oncol*. 2018;127:S533-S534.
12. Sarosiek C, DeJongh EA, Coutrakon G, et al. Analysis of characteristics of images acquired with a prototype clinical proton radiography system. *Med Phys*. 2021;48:2271-2278.
13. Deffet S, Cohilis M, Souris K, et al. openPR - a computational tool for CT conversion assessment with proton radiography. *Med Phys*. 2021;48:387-396.
14. Schneider U, Pedroni E. Proton radiography as a tool for quality control in proton therapy. *Med Phys*. 1995;22:353-363.
15. Hammi A, Placidi L, Weber DC, Lomax AJ. Positioning of head and neck patients for proton therapy using proton range probes: a proof of concept study. *Phys Med Biol*. 2017;63:015025.
16. Hammi A, Koenig S, Weber DC, Poppe B, Lomax AJ. Patient positioning verification for proton therapy using proton radiography. *Phys Med Biol*. 2018;63:245009.
17. Mumot M, Algranati C, Hartmann M, Schippers JM, Hug E, Lomax AJ. Proton range verification using a range probe: definition of concept and initial analysis. *Phys Med Biol*. 2010;55:4771-4771.
18. Miller C, Altoos B, DeJongh EA, et al. Reconstructed and real proton radiographs for image-guidance in proton beam therapy. *J Radiat Oncol*. 2019;8:97-101.
19. Collins-Fekete CA, Dikaios N, Royle G, Evans PM. Statistical limitations in proton imaging. *Phys Med Biol*. 2020;65:085011.
20. Gehrke T, Gallas R, Jäkel O, Martišíková M. Proof of principle of helium-beam radiography using silicon pixel detectors for energy deposition measurement, identification, and tracking of single ions. *Med Phys*. 2018;45:817-829.
21. Gehrke T, Amato C, Berke S, Martišíková M. Theoretical and experimental comparison of proton and helium-beam radiography using silicon pixel detectors. *Phys Med Biol*. 2018;63:035037.
22. Amato C, Martišíková M, Gehrke T. A technique for spatial resolution improvement in helium-beam radiography. *Med Phys*. 2020;47.
23. Bashkirov VA, Schulte RW, Hurley RF, et al. Novel scintillation detector design and performance for proton radiography and computed tomography. *Med Phys*. 2016;43:664-674.
24. Volz L, Piersimoni P, Johnson RP, Bashkirov VA, Schulte RW, Seco J. Improving single-event proton CT by removing nuclear interaction events within the energy/range detector. *Phys Med Biol*. 2019;64:15NT01.
25. Pettersen HES, et al. Helium radiography with a digital tracking calorimeter—a Monte Carlo study for secondary track rejection. *Phys Med Biol*. 2021;66:035004.
26. Hansen DC, Bassler N, Sørensen TS, Seco J. The image quality of ion computed tomography at clinical imaging dose levels. *Med Phys*. 2014;41:111908.
27. Collins-Fekete CA, Volz L, Portillo SK, Beaulieu L, Seco J. A theoretical framework to predict the most likely ion path in particle imaging. *Phys Med Biol*. 2017;62:1777-1790.
28. Piersimoni P, Faddegon BA, Mendez JR, Schulte RW, Volz L, Seco J. Helium CT: Monte Carlo simulation results for an ideal source and detector with comparison to proton CT. *Med Phys*. 2018;45:3264-3274.
29. Volz L, Collins-Fekete C-A, Piersimoni P, et al. Stopping power accuracy and achievable spatial resolution of helium ion imaging using a prototype particle CT detector system. *Curr Dir Biomed Eng*. 2017;3:401.
30. Volz L, Piersimoni P, Bashkirov VA, et al. The impact of secondary fragments on the image quality of helium ion imaging. *Phys Med Biol*. 2018;63.
31. Kopp B, Meyer S, Gianoli C, et al. Experimental comparison of clinically used ion beams for imaging applications using a range telescope. *Phys Med Biol*. 2020;65:155004.
32. Volz L, Collins-Fekete C-A, Bär E, et al. The accuracy of helium ion CT based particle therapy range prediction: an experimental study comparing different particle and X-ray CT modalities. *Phys Med Biol*. 2021;66:235010.
33. Dickmann J, Sarosiek C, Götz S, et al. An empirical artifact correction for proton computed tomography. *Phys Med*. 2021;86:57-65.
34. Llopart X, Ballabriga R, Campbell M, Tlustos L, Wong W. Timepix, a 65k programmable pixel readout chip for arrival time, energy and/or photon counting measurements. *Nucl Instrum Methods Phys Res*. 2007;581:485.
35. Granja C, Jakubek J, Polansky S, et al. Resolving power of pixel detector Timepix for wide-range electron, proton and ion detection. *Nucl Instrum Methods Phys Res, Sect A*. 2018;908:60-71.
36. Jakubek J. Precise energy calibration of pixel detector working in time-over-threshold mode. *Nucl Instrum Methods Phys Res, Sect A*. 2011;633:S262-S266.
37. Gehrke T, Burigo L, Arico G, et al. Energy deposition measurements of single 1 H, 4 He and 12 C ions of therapeutic energies in a silicon pixel detector. *J Instrum*. 2017;12:P04025.
38. Berger MJ, Coursey JS, Zucker MA, Chang J. ESTAR, PSTAR, and ASTAR: Computer Programs for Calculating Stopping-Power and Range Tables for Electrons, Protons, and Helium Ions (version 1.2.3).
39. Kraus V, Holik M, Jakubek J, Kroupa M, Soukup P, Vykydal Z. FITPix — fast interface for Timepix pixel detectors. *J Instrum*. 2011;6:C01079.
40. Haberer T, Debus J, Eickhoff H, Jäkel O, Schulz-Ertner D, Weber U. The Heidelberg ion therapy center. *Radiother Oncol*. 2004;73:S186-S190.

41. Eickhoff H, Bar R, Dolinskii A, et al. HICAT - the German hospital-based light ion cancer therapy project. In *Proceedings of the 2003 Particle Accelerator Conference*. 2003;1:694-698.

42. Dolinskii A, Eickhoff H, Franczak B. The synchrotron of the dedicated ion beam facility for cancer therapy, proposed for the clinic in Heidelberg. In *Proceedings of EPAC 2000*. Austria: Vienna; 2000.

43. Schultze B, Karbasi P, Sarosiek C, et al. Particle-tracking proton computed tomography–data acquisition, preprocessing, and preconditioning. *IEEE Access*. 2021;9:25946-25958.

44. Schulte RW, Penfold SN, Tafas JT, Schubert KE. A maximum likelihood proton path formalism for application in proton computed tomography. *Med Phys*. 2008;35:4849-4856.

45. Williams DC. The most likely path of an energetic charged particle through a uniform medium. *Phys Med Biol*. 2004;49:2899-2911.

46. Schneider U, Pedroni E. Multiple Coulomb scattering and spatial resolution in proton radiography. *Med Phys*. 1994;21:1657-1663.

47. Fekete CAC, Doolan P, Dias MF, Beaulieu L, Seco J. Developing a phenomenological model of the proton trajectory within a heterogeneous medium required for proton imaging. *Phys Med Biol*. 2015;60:5071-5082.

48. Collins-Fekete C-A, Volz L, Portillo SKN, Beaulieu L, Seco J. A theoretical framework to predict the most likely ion path in particle imaging. *Phys Med Biol*. 2017;62:1777-1790.

49. Krah N, Létang JM, Rit S. Polynomial modelling of proton trajectories in homogeneous media for fast most likely path estimation and trajectory simulation. *Phys Med Biol*. 2019;64:195014.

50. Collins-Fekete C-A, Brousmiche S, Portillo SKN, Beaulieu L, Seco J. A maximum likelihood method for high resolution proton radiography/proton CT. *Phys Med Biol*. 2016;61:8232-8248.

51. Schneider U, Besserer J, Pemler P, et al. First proton radiography of an animal patient. *Med Phys*. 2004;31:1046-1051.

52. Volz L, Collins-Fekete CA, Sølie JR, Seco J. Theoretical considerations on the spatial resolution limit of single-event particle radiography. *Bio Med Phys Eng Express*. 2020;6:055002.

53. Lühr A, Toftegaard J, Kantemiris I, Hansen DC, Bassler N. Stopping power for particle therapy: the generic library libdEdx and clinically relevant stopping-power ratios for light ions. *Int J Radiat Biol*. 2012;88:209-212.

54. Hall C. *Laws and Models: Science, Engineering, and Technology*. CRC Press; 2000.

55. Bortfeld T. An analytical approximation of the Bragg curve for therapeutic proton beams. *Med Phys*. 1997;24:2024-2033.

56. Dickmann J, Wesp P, Rädler M, et al. Prediction of image noise contributions in proton computed tomography and comparison to measurements. *Phys Med Biol*. 2019;64:145016.

57. Chu WT, Ludewigt BA, Renner TR. Instrumentation for treatment of cancer using proton and light-ion beams. *Rev Sci Instrum*. 1993;64:2055-2122.

58. Pirruccello M, Tobias C. Biological and Medical Research with Accelerated Heavy Ions at the Bevalac. 1977–1980. *Report*. Lawrence Berkeley National Laboratory; 1980.

59. Mori I, Machida Y. Deriving the modulation transfer function of CT from extremely noisy edge profiles. *Radiol Phys Technol*. 2009;2:22-32.

60. Judy PF. The line spread function and modulation transfer function of a computed tomographic scanner. *Med Phys*. 1976;3:233-236.

61. Seco J, Oumano M, Depauw N, Dias MF, Teixeira RP, Spadea MF. Characterizing the modulation transfer function (MTF) of proton/carbon radiography using Monte Carlo simulations. *Med Phys*. 2013;40:091717.

62. Plautz TE, Bashkirov V, Giacometti V, et al. An evaluation of spatial resolution of a prototype proton CT scanner. *Med Phys*. 2016;43:6291-6300.

63. Schömers C, Feldmeier E, Galonska M, Haberer T, Horn J, Peters A. First Tests of a Re-accelerated Beam at Heidelberg Ion-Beam Therapy Centre (HIT). 2017.

64. Poikela T, Plosila J, Westerlund T, et al. Timepix3: a 65K channel hybrid pixel readout chip with simultaneous ToA/ToT and sparse readout. *J Instrum*. 2014;9:C05013.

65. Llopart X, Alozy J, Ballabriga R, et al. Timepix4, a large area pixel detector readout chip which can be tiled on 4 sides providing sub-200 ps timestamp binning. *J Instrum*. 2022;17: C01044.

66. Liermann J, Naumann P, Hommertgen A, et al. Carbon ion radiotherapy as definitive treatment in non-metastasized pancreatic cancer: study protocol of the prospective phase II PACK-study. *BMC Cancer*. 2020;20:947.

67. Arians N, Lindel K, Krisam J, et al. Prospective phase-II-study evaluating postoperative radiotherapy of cervical and endometrial cancer patients using protons - the APROVE-trial. *Radiat Oncol*. 2017;12:188.

68. Bär B, Volz L, Collins-Fekete CA, et al. Experimental comparison of photon versus particle computed tomography to predict tissue relative stopping powers. *Med Phys*. 2022;49:474-487.